


## Article

# Investigation of Mineral Phase Transformation Technology Followed by Magnetic Separation for Recovery of Iron Values from Red Mud

Shuai Yuan <sup>1</sup>, Ruofeng Wang <sup>1,\*</sup> , Hao Zhang <sup>1</sup>, Yanjun Li <sup>1</sup>, Liu Liu <sup>2</sup> and Yafeng Fu <sup>2</sup><sup>1</sup> College of Resources and Civil Engineering, Northeastern University, Shenyang 110819, China<sup>2</sup> Ansteel Beijing Research Institute Co., Ltd., Beijing 102200, China

\* Correspondence: ruofeng572725@163.com; Tel.: +86-18332723577

**Abstract:** Experiments were conducted to investigate the mineral phase transformation technology of high-iron red mud, effectively extracting valuable iron minerals and reducing the hazards associated with red mud stockpiling and storage. A magnetic concentrate with an iron grade of 55.84% and recovery of 93.75% could be obtained at a roasting temperature of 560 °C, roasting time of 15 min, CO concentration of 20% and total gas flow of 500 mL/min. A combination of XRD and SEM-EDS analysis was employed to evaluate the phase transformation during the roasting process. ToF-SIMS analysis was applied to assess the occurrence state of various elements during the roasting of red mud.

**Keywords:** red mud; mineral phase transformation; magnetic separation; roasting



check for updates

**Citation:** Yuan, S.; Wang, R.; Zhang, H.; Li, Y.; Liu, L.; Fu, Y. Investigation of Mineral Phase Transformation Technology Followed by Magnetic Separation for Recovery of Iron Values from Red Mud. *Sustainability* **2022**, *14*, 13787. <https://doi.org/10.3390/su142113787>

Academic Editors: Saeed Chehreh Chelgani and Anna Młynarczykowska

Received: 28 August 2022

Accepted: 21 October 2022

Published: 24 October 2022

**Publisher's Note:** MDPI stays neutral with regard to jurisdictional claims in published maps and institutional affiliations.



**Copyright:** © 2022 by the authors. Licensee MDPI, Basel, Switzerland. This article is an open access article distributed under the terms and conditions of the Creative Commons Attribution (CC BY) license (<https://creativecommons.org/licenses/by/4.0/>).

## 1. Introduction

Red mud (RM) is a strong alkaline solid waste produced in alumina production; it mainly contains alumina, iron oxide, sodium oxide, titanium dioxide and other components and varies in color from red to off-white due to the varying iron oxide content [1–4]. As of 2021, the world's red mud reserves exceeded four billion tons and continue to grow at a frantic rate of 175.5 million per year [5,6], resulting in increasing soil alkalization problems and environmental damage from groundwater pollution. The hazards caused by red mud are shown in Figure 1. China, the world's largest producer of alumina and RM, has amassed over 600 million tons of RM [7,8]. Typically, large quantities of RM are often located in specially constructed open spaces, which poses an environmental risk on account of the hazardous effects of their high alkaline content; they have been summarized in the European Waste Catalog (EWC) and the Hazardous Waste List [9–12]. In response to national attention on environmental issues, the environmentally sound treatment of red mud and its bulk consumption and utilization has long been a priority [13].

Red mud particles have a fine morphology, generally between 5 and 75 µm in diameter, with a much higher specific surface area and porosity than ordinary soil [1,12]. The excellent dispersion and solution stability of red mud particles make them particularly favored in environmental management, where they are often used as low-cost adsorbents for waste gas and wastewater treatment and as catalysts for catalytic reactions [14–16]. In construction materials and their related fields, RM is widely used to prepare high-porosity bricks and class-ceramic or subgrade materials, as its chemical composition is similar to silicate cement [17]. Some scholars have also studied the preparation of cement with RM, which unfortunately leads to a loss of minerals [18,19]. Large amounts of residual minerals (hematite, rutile and quartz) in RM at significant metal concentrations make it a potential polymetallic source. Attempts to recover aluminum, iron, sodium and other valuable elements from RM are of substantial relevance in dealing with the concerns associated with these solid wastes, particularly considering the rising iron ore prices and the scarcity of rare earth supplies worldwide [20,21].

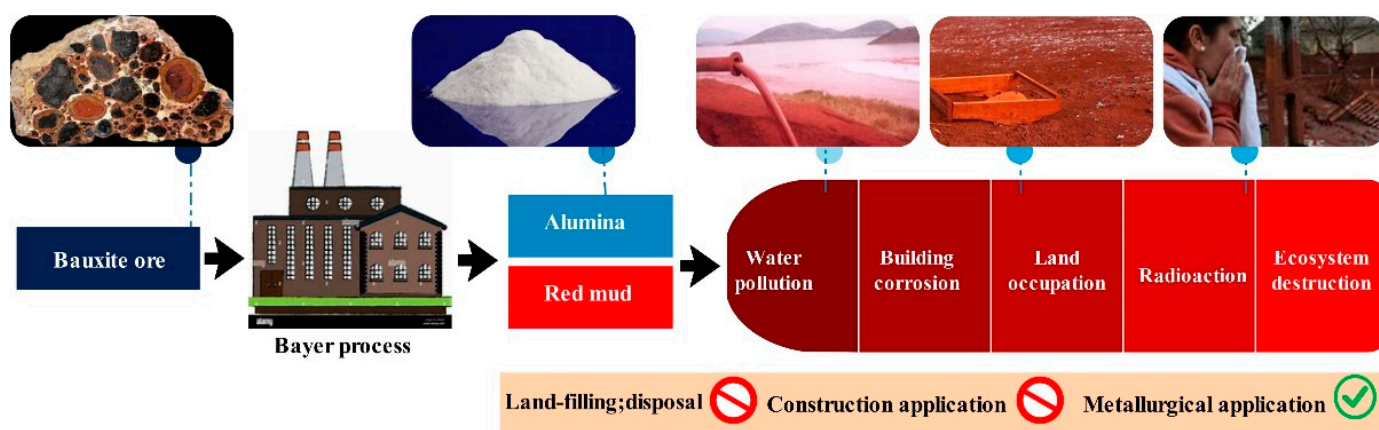


Figure 1. The hazards caused by red mud.

Iron is the main component of red mud, expressed mainly as hematite and goethite, especially for high-iron RM, which can even be regarded as an iron resource. However, iron resources are hardly concentrated due to their complex composition and fine particle size [22]. Numerous researchers have recently investigated methods of recovering iron from RM in recent years. These methods can generally be summarized as physical separation, hydrometallurgy, pyrometallurgy or some combination of the above methods. The main physical separation methods for recovering iron from RM include high-intensity magnetic separation and gravity separation [23,24]. Hydrometallurgy methods are when iron or other metallic elements are dissolved and retrieved in an acid leaching process (hydrochloric acid, sulfuric acid, phosphoric acid and nitric acid) [25–27]. The pyrometallurgical method can mainly be divided into reduction smelting and roasting methods. The recovery of metallic minerals is achieved by reducing weakly magnetic hematite and goethite to magnetite or metallic Fe [28,29]. To date, it has been considered a popular method for recycling iron from RM. However, given the disadvantages of the conventional roasting process, such as serious environmental pollution and low recovery, an innovative mineral phase transformation technology is proposed to extract iron from red mud effectively. The mineral phase transformation technology is based on the basic principle of fluidization technology. The ore is suspended under airflow action, exploiting the contact between the hot airflow and the ore particles to accelerate the roasting reaction.

This paper reports the treatment of RM by mineral phase transformation-magnetic separation technology to obtain roasted products under optimum conditions through variations in the magnetic concentrate index. Time-of-flight mass spectrometry (ToF-SIMS) was employed to analyze samples to investigate the occurrence state of various elements during the roasting process. X-ray diffraction and scanning electron microscopy-energy spectrometry (SEM-EDS) analysis were used to analyze and compare the samples in detail to elucidate the distribution of various elements in the samples. The above investigations enriched the basic theoretical system of high-iron red mud, allowing the targeted and synergistic extraction of valuable components.

## 2. Materials and Methods

### 2.1. Analytical Techniques

#### 2.1.1. X-ray Diffraction Analysis

X-ray diffraction analysis is a technique for material structure analysis using the diffraction effect of X-rays in crystalline materials. The crystal structure of the sample was studied by XRD (PW3040, Netherlands), and the sample was scanned between  $5^\circ$  and  $90^\circ$  at a rate of  $12^\circ/\text{min}$  over a range of  $2\theta$ . The instrument parameters were as follows: Cu target radiation, Ni filter, pipe voltage of 45 kV, pipe current of 200 mA, incoming ray wavelength of  $1.541 \text{ \AA}$  and working temperature of  $25^\circ\text{C}$ .

### 2.1.2. Magnetic Analysis

A vibrating sample magnetometer (VSM) can measure the magnetic properties of magnetic materials. This study used the JDAW-2000D model vibrating sample magnetometer produced by Changchun Yingpu Magnetolectric Technology Development Co., Ltd., Changchun, China. The working parameters were as follows: the magnetic moment range was 8 emu/g, the sample mass was 50 mg and the external magnetic field strength was 800 kA/m.

### 2.1.3. Scanning Electron Microscope Analysis

Scanning electron microscopy (SEM) (ULTRA PLUS, Zeiss, Germany) was used to evaluate the microstructural evolution of minerals during mineral phase transformation. The mineral particles were embedded and fixed with epoxy resin; grinding and polishing were conducted to prepare for the SEM analysis. In this study, the field emission scanning electron microscope's resolution could reach 0.8 nm at 15 kV and 1.6 nm at 1 kV. The magnification could reach 1 million times, and the acceleration voltage was 20 V~30 kV.

### 2.1.4. ToF-SIMS Analysis

Time-of-flight secondary mass spectrometry (TOF-SIMS) is a surface-sensitive analysis technique that enables qualitative analysis of the surface chemical composition and mapping distribution of target elements for various unknown substances. The instrument used in this research was the TOF.SIMS 5–100 model time-of-flight secondary mass spectrometer manufactured by ION-TOF GmbH, Germany. The positive ion sputtering beam adopted the  $O_2^+$  ion beam generated by 1 keV charged  $O_2$ , and the incident angle was 45 deg. The negative ion sputtering beam was a  $Cs^+$  ion beam produced by 1 keV charged Cs with an incident angle of 45 deg.

## 2.2. Materials

In this study, the red mud was collected from Shandong, China, referred to as raw ore. X-ray diffraction (XRD) was used to analyze the main phase composition, and the results are presented in Figure 2. The main crystalline minerals in the high-iron RM were hematite, goethite, ilmenite, diaspore and other minerals, among which the hematite diffraction peaks showed a high intensity, indicating the presence of a large number of iron minerals in the raw ore suitable for recycling.

The chemical composition of the red mud is given in Table 1. The representative raw ore comprised 47.47% Fe, 12.14%  $Al_2O_3$ , 4.14%  $TiO_2$  and 1.12%  $Na_2O$ .

**Table 1.** Analysis of chemical composition of raw ore (mass fraction, %).

<b>Component</b>	<b>TFe</b>	<b>FeO</b>	<b>SiO<sub>2</sub></b>	<b>Al<sub>2</sub>O<sub>3</sub></b>	<b>TiO<sub>2</sub></b>
Counts	47.47	0.12	1.94	12.14	4.14
<b>Component</b>	<b>P</b>	<b>S</b>	<b>K<sub>2</sub>O</b>	<b>CaO</b>	<b>LOI</b>
Counts	0.07	0.026	0.05	0.37	11.11

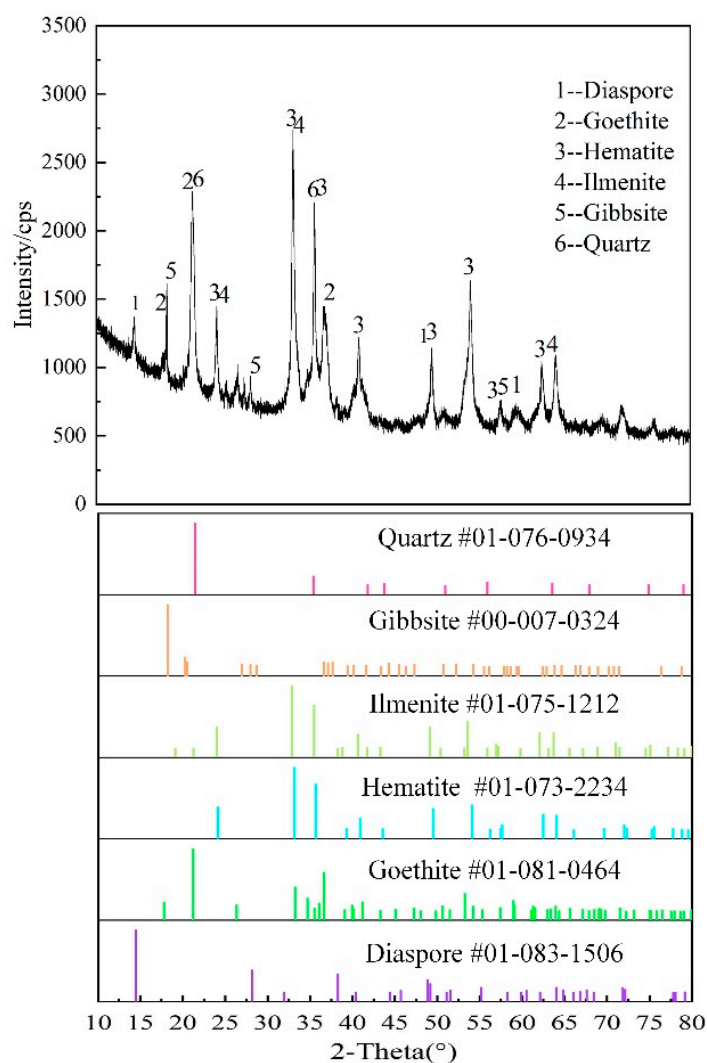


**Figure 2.** XRD pattern of red mud raw ore.

The chemical iron phase analysis results on the investigated RM are shown in Table 2. The results demonstrated that a significant concentration of iron minerals was present in the raw ore, with the vast majority being found in the hematite/limonite, where the distribution reached 98.44%.

**Table 2.** Chemical iron phase analysis of raw ore (mass fraction, %).

Content	Fe in Magnetite	Fe in Carbonate	Fe in Hematite	Fe in Sulfide	Fe in Silicate	Total
Distribution	0.35	0.08	46.6	0.20	0.38	47.67
Content	0.73	0.17	97.88	0.42	0.80	100.00

### 2.3. The Technical Route of RM Utilization

The RM raw ore was reddish-brown argillaceous siltstone with a fine particle size without grinding and could be used after mixing. A laboratory high-temperature furnace was established (Figure 3), the roasting temperature was set and 500 mL/min nitrogen gas was introduced as a protective gas. Fifteen grams of raw ore was placed in a quartz tube to cover the porous quartz plate as uniformly as possible and to suspend the RM particles under the action of the gas flow, showing fluidization characteristics and enhancing the contact between the gas and the particles. Roasting experiments were carried out



by adjusting the reducing gas to nitrogen ratio. After the investigations, the roasted products were separated with a magnetic separator, and the magnetic concentrates obtained were analyzed. The iron grade of the sample was determined by chemical analysis with potassium dichromate titration, and the iron recovery was calculated using Equation (1).

$$\text{Iron recovery} = \frac{\text{weight of samples} \times \text{iron grade of samples}}{\text{weight of raw ore} \times \text{iron grade of raw ore}} \times 100\% \quad (1)$$

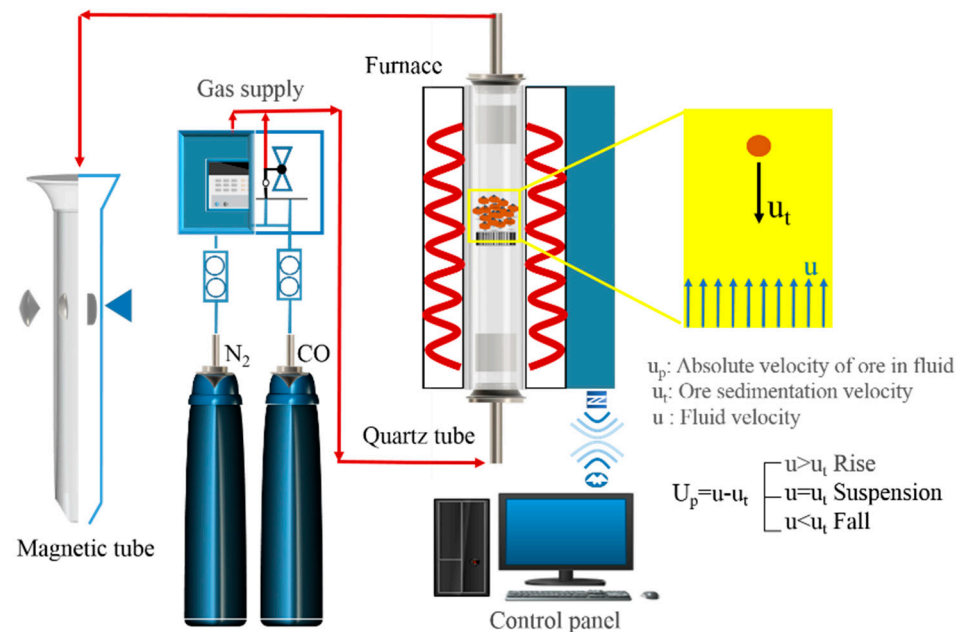


Figure 3. Schematic diagram of the principle of the laboratory high-temperature furnace.

### 3. Results and Discussion

This study evaluated the effectiveness of mineral phase transformation technology. The optimum experimental conditions for the roasting of red mud were determined by analyzing the indicators of iron grade and recovery of the magnetic concentrate, combined with the analysis of the saturation magnetization of the roasted products.

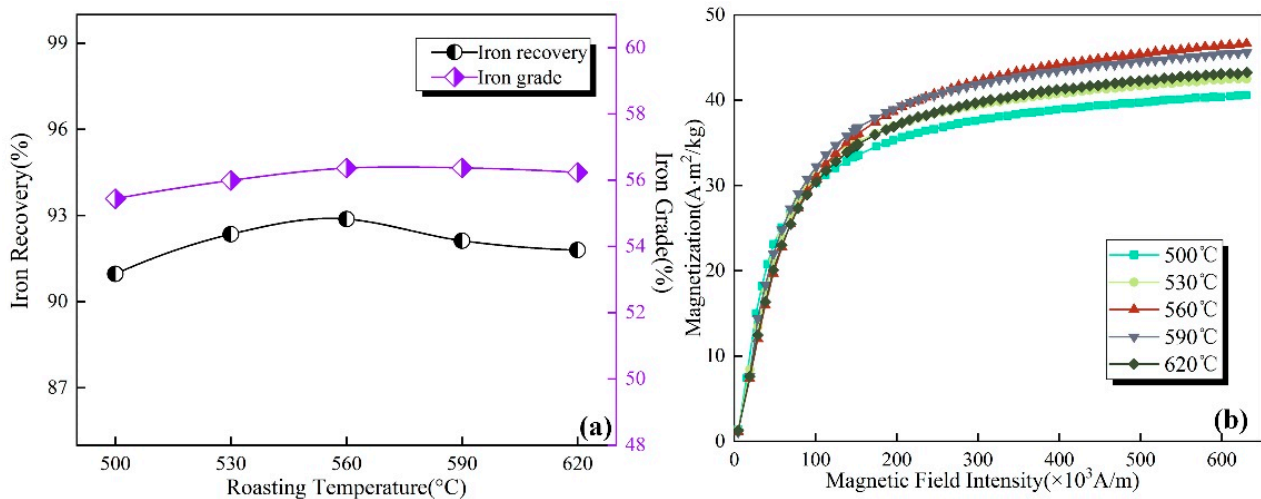
#### 3.1. Effects of Roasting Temperature

The effect of temperature on the experimental results was investigated with a total gas flow rate of 500 mL/min and 20% CO concentration. The temperature was controlled in the range of 500–620 °C at intervals of 30 °C for 15 min. The obtained roasted product was cooled to room temperature in an N<sub>2</sub> atmosphere, followed by magnetic separation at a magnetic field strength of 87.54 kA/m for 5 min. The effect of roasting temperature on the index of the magnetic concentrate is illustrated in Figure 4a. The saturation magnetization of the roasted products with different roasting temperatures is displayed in Figure 4b.

Figure 4a indicates that the roasting temperature significantly affected the roasting process. Noticeable magnetic concentrate index fluctuations were observed within the temperature range tested. At the same time, the iron grade increased from 55.44% to 56.36% and the iron recovery increased from 90.96% to 92.87% from 500 °C to 560 °C. Then, the iron grade decreased slightly to 56.23% and the iron recovery dropped to 91.79% as the temperature rose to 620 °C.

Compared with the results shown in Figure 4a, the influence of roasting temperature on the saturated magnetization in the roasted products exhibited the same trend. The saturation magnetization intensity (Figure 4b) increased and peaked at 560 °C. The maximum saturation magnetization was 46.62 A·m<sup>2</sup>/kg. The saturation magnetization intensity decreased to 43.24 A·m<sup>2</sup>/kg when the roasting temperature was further increased to

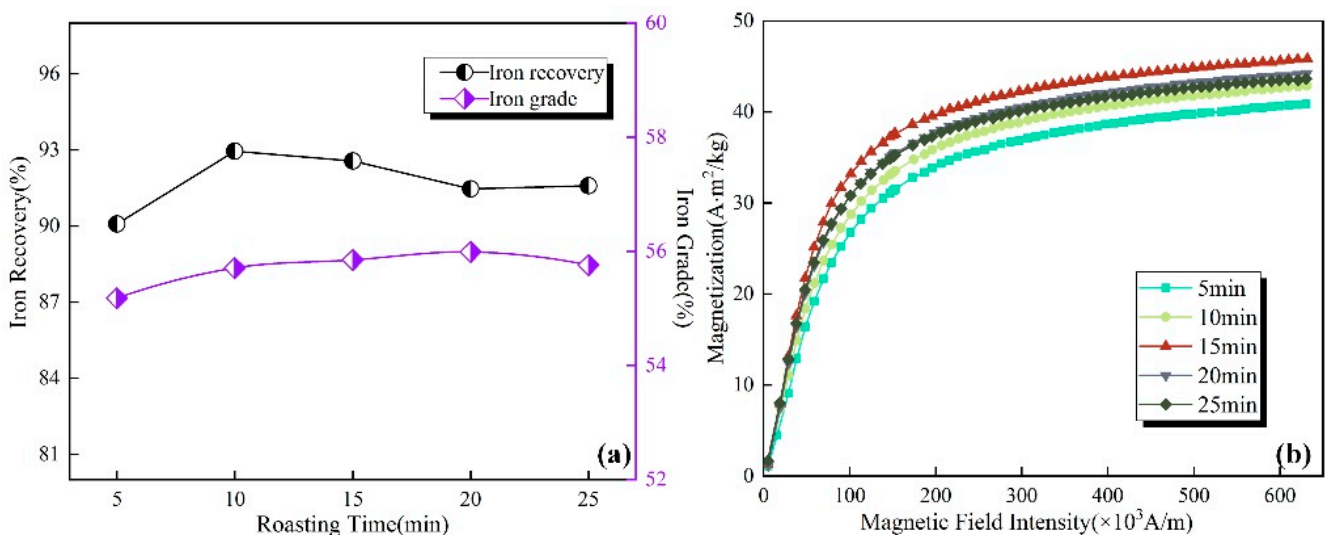
620 °C. This can be explained by the fact that the content of the generated strongly magnetic magnetite increased continuously with increasing roasting temperature. However, when the roasting temperature was increased to 560 °C, the magnetite in the roasted product began to transform into weaker magnetic wustite, resulting in a decrease in the saturation magnetization intensity of the roasted product and weakening the sample magnetism [30]. Therefore, it was determined that the optimal roasting temperature was 560 °C.



**Figure 4.** Effect of roasting temperature on (a) the index of the magnetic concentrate and (b) the saturation magnetization of roasted product.

### 3.2. Effects of Roasting Time

The effects of roasting time on the index of the magnetic concentrate were studied under the following parameters: roasting temperature of 560 °C, total gas flow rate of 500 mL/min and CO concentration of 20%; the results are shown in Figure 5a.



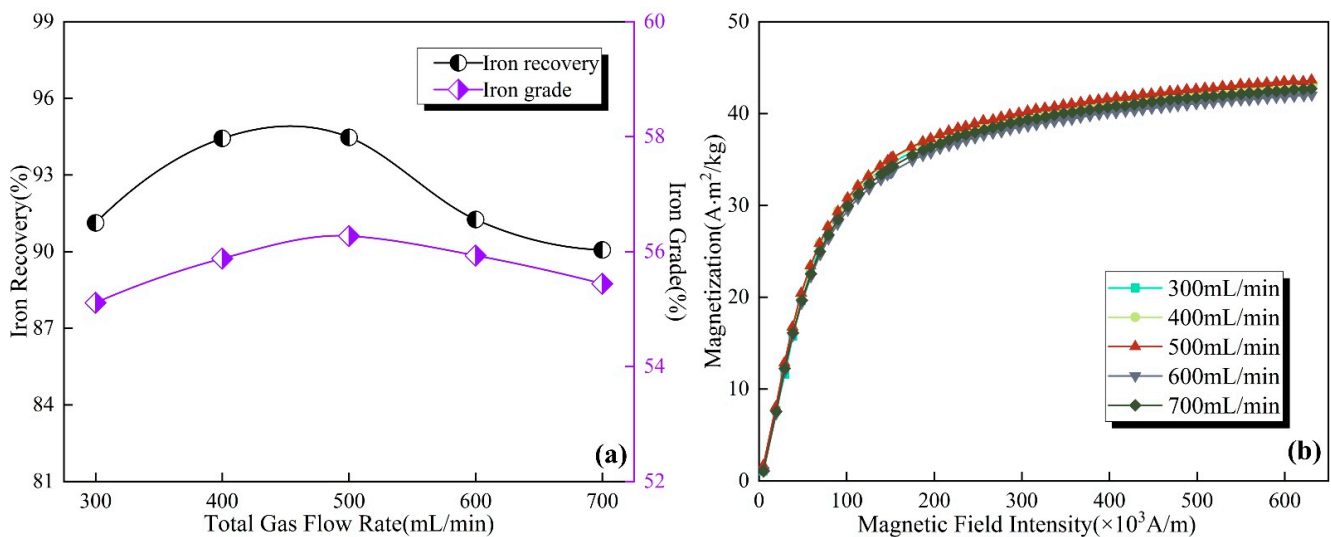
**Figure 5.** Effect of roasting time on (a) the index of the magnetic concentrate and (b) the saturation magnetization of roasted product.

Figure 5a demonstrates that as the roasting time increased, the iron grade and iron recovery of the magnetic concentrate showed a single-peaked trend of increasing and then decreasing. The iron grade in the magnetic concentrate rose from 55.18% to 55.99% and then fell to 55.76%, with the iron grade reaching the peak value at 20 min. The iron recovery of the concentrate was the highest at the roasting time of 10 min, which was 92.94%.

As shown in Figure 5b, when the roasting time was increased from 5 min to 15 min, the saturation magnetization intensity of the roasted products increased from  $40.87 \text{ A}\cdot\text{m}^2/\text{kg}$  to  $45.85 \text{ A}\cdot\text{m}^2/\text{kg}$ ; then, when we increased the roasting time to 25 min, the saturation magnetization intensity decreased to  $43.64 \text{ A}\cdot\text{m}^2/\text{kg}$ . Therefore, after comprehensive consideration, the optimal time was determined to be 15 min, at which time the iron grade of the magnetic concentrate was 55.85% and the iron recovery was 92.56%.

### 3.3. Effects of Total Gas Flow Rate

In the roasting process, the gas was fed into the roaster from the bottom upwards, during which the roasted samples reached a suspended fluidized state, and there was sufficient contact and reaction between the reducing gas and the ore. Under the conditions of a roasting temperature of  $560 \text{ }^\circ\text{C}$ , a roasting time of 15 min and a CO concentration of 20%, the effects of the total gas flow rate on the magnetic concentrate index were studied and are presented in Figure 6a.



**Figure 6.** Effect of total gas flow rate on (a) the index of the magnetic concentrate and (b) the saturation magnetization of roasted product.

The samples could not be effectively dispersed and loosened at the low gas flow rate, resulting in insufficient contact between the gas molecules and the mineral particles, which prevented the reduction reaction. However, the high gas flow rate caused the fine particles to be blown out of the roaster, resulting in sample loss. According to Figure 6a, at a total gas flow rate of 500 mL/min, the magnetic concentrate with an iron grade of 56.27% and iron recovery of 94.47% achieved the peak value.

The saturation magnetization intensity analysis conducted by VSM, shown in Figure 6b, showed that the plots increased and peaked with a gas flow rate of 500 mL/min and then decreased when the gas flow rate increased further. Therefore, a total gas flow rate of 500 mL/min was selected as the optimum condition for the subsequent experimental study.

### 3.4. Effects of CO Concentration

CO concentration is one of the main factors affecting the reduction of iron minerals. The effect of CO concentration on the index of the magnetic concentrate was investigated by applying CO concentrations from 10% to 50%. The experiments were performed with a roasting temperature of  $560 \text{ }^\circ\text{C}$ , a roasting time of 15 min and a total gas flow rate of 500 mL/min, and the results are given in Figure 7a.

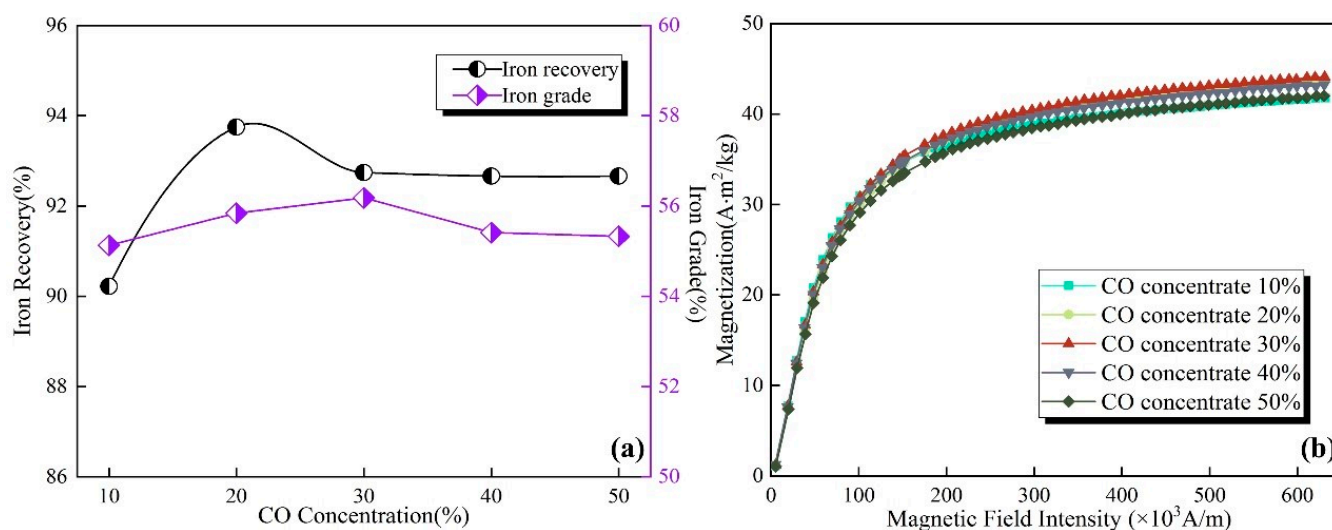


**Figure 7.** Effect of CO concentration on (a) the index of the magnetic concentrate and (b) the saturation magnetization of roasted product.

As seen in Figure 7a, iron grade varied slightly, ranging from 55.15% to 56.18%. The iron recovery increased from 90.21% to 93.75% as the CO concentration changed from 10% to 20% and then decreased to 92.68% at a CO concentration of 50%. The incomplete transformation of hematite to magnetite at low CO concentrations, over-reduction at high CO concentrations and further reaction of newly formed magnetite with excess CO gas generate FeO [31].

According to Figure 7b, the saturation magnetization intensity of the roasted product increased from 41.74 A·m<sup>2</sup>/kg to 44.09 A·m<sup>2</sup>/kg when the CO concentration increased from 10% to 30% and then decreased to 42.01 A·m<sup>2</sup>/kg when the CO concentration was increased to 50%. The optimal CO concentration was determined to be 20% to ensure the recovery of iron minerals. Finally, a magnetic concentrate with an iron grade of 55.84% and a recovery of 93.75% and a tailing with an iron grade of 14.62% and a recovery of 6.25% were obtained under the optimal roasting conditions.

### 3.5. Phase Transformation

The samples in different roasting-separation stages under the optimal experimental conditions were investigated in detail, and the results of XRD are presented in Figure 8. Figure 8 shows that the diffraction peaks of goethite and hematite in the raw ore disappeared after roasting. In contrast, diffraction peaks corresponding to magnetite appeared, indicating that hematite was selectively transformed into magnetite. Strong magnetite peaks were discovered in the magnetic concentrate. Iron titanium oxide, quartz and Al<sub>2</sub>O<sub>3</sub> as well as silicate minerals such as pyroxene and andradite were enriched in the magnetic tailings. Meanwhile, Fe-Al spinel phase Fe(Al, Fe)<sub>2</sub>O<sub>4</sub> was found in the magnetic concentrate and tailings. No diffraction peaks corresponded to magnetite in the magnetic tailings. This shows that it is feasible and effective to use mineral phase transformation technology to transform the iron mineral phase and certifies the success of separating magnetite and gangue minerals by magnetic separation.

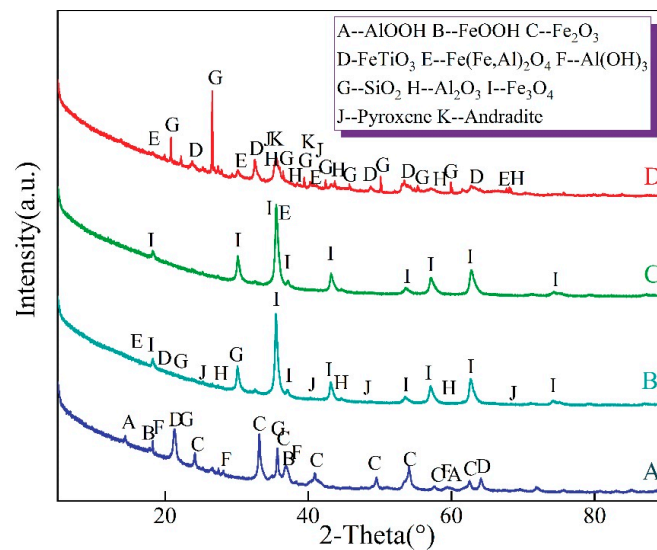


**Figure 8.** XRD pattern analysis of samples in different roasting-separation stages: (A) raw ore, (B) roasted product, (C) magnetic concentrate and (D) magnetic tailings.

### 3.6. ToF-SIMS Analysis

Time-of-flight secondary ion mass spectrometry (ToF-SIMS) is already considered a relevant and highly sensitive technique to obtain samples' elemental and chemical depth profiles [32–35]. Mass spectra provide detailed elemental and molecular information on the outermost layer of the sample surface, as shown in Figures 9 and 10.

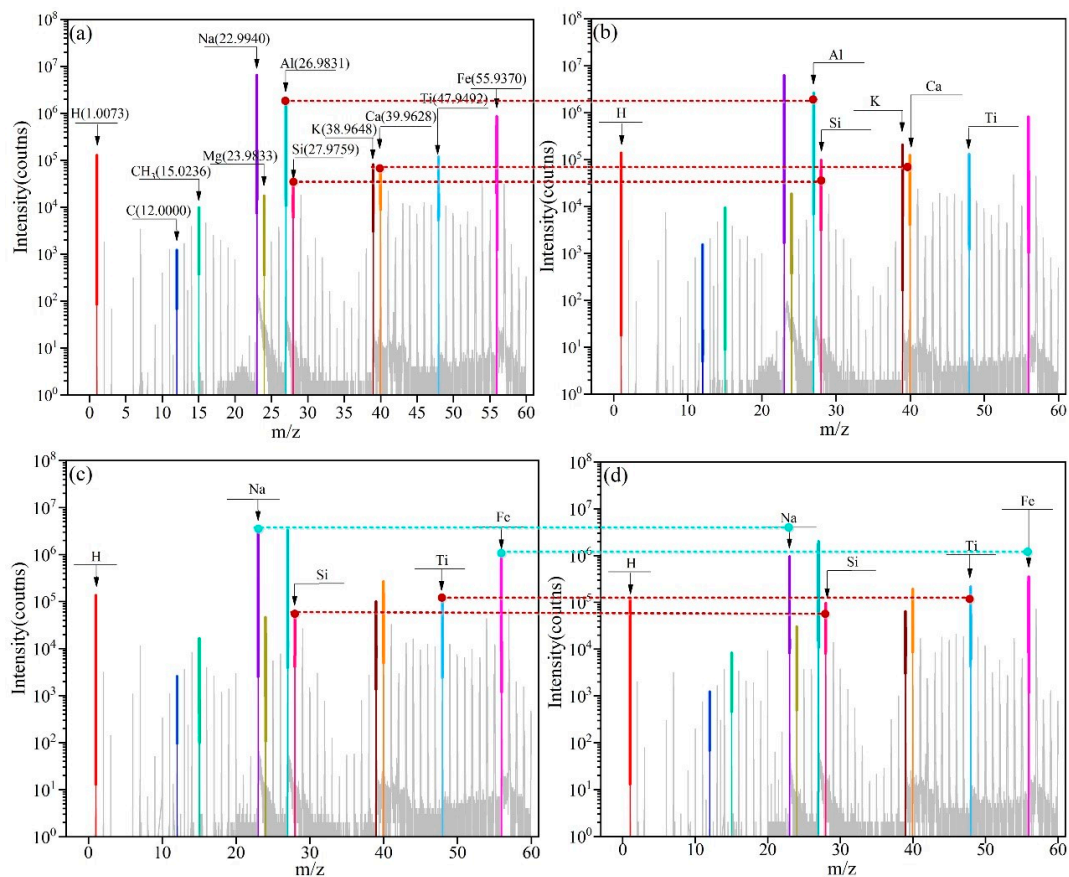


**Figure 9.** ToF-SIMS (0–60 m/z) positive ion mass spectra of (a) raw ore, (b) roasted product, (c) magnetic concentrate and (d) magnetic tailings.



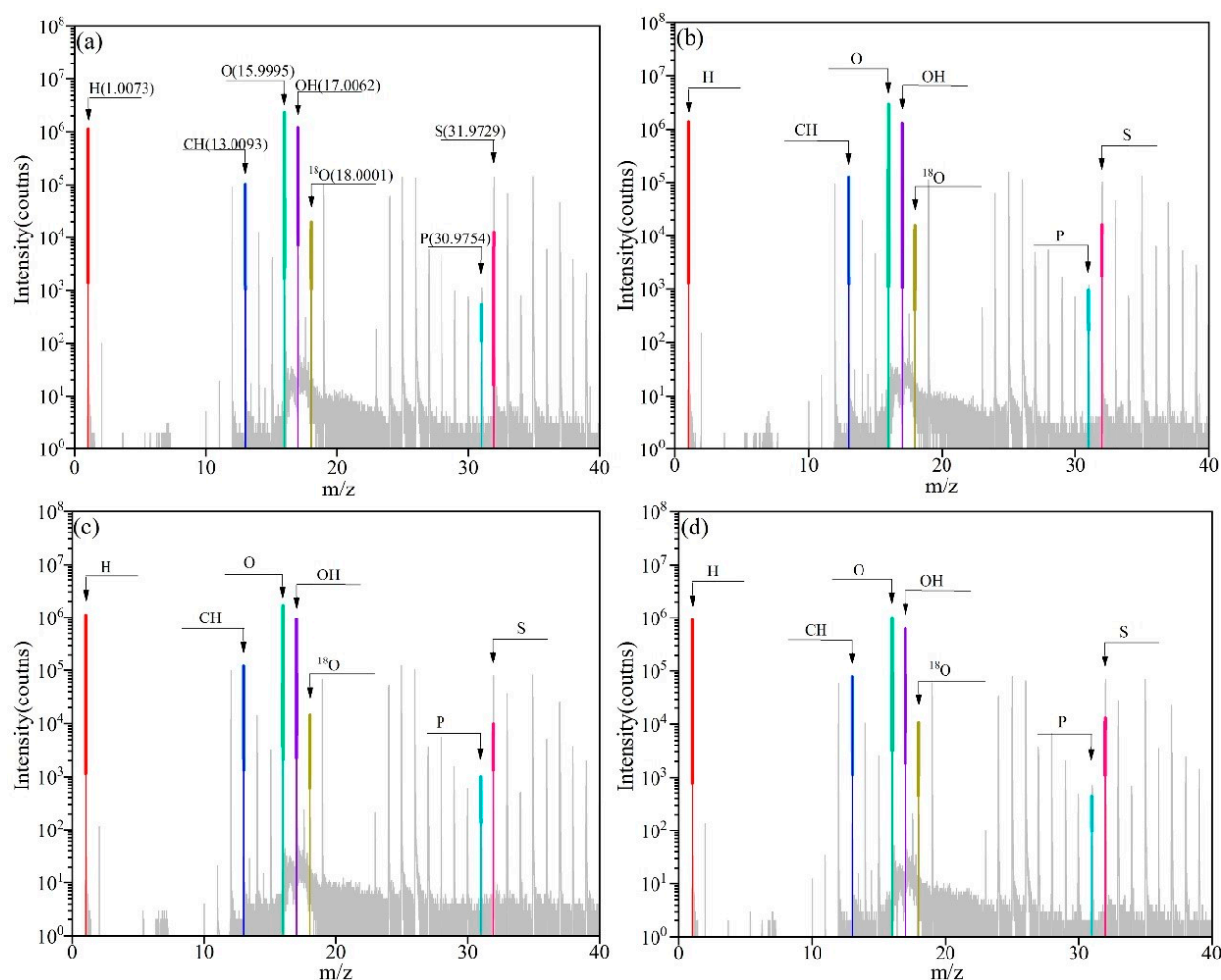


**Figure 10.** ToF-SIMS (0~40 m/z) negative ion mass spectra of (a) raw ore, (b) roasted product, (c) magnetic concentrate and (d) magnetic tailings.

Figure 9 presents the positive ion ToF-SIMS spectra for samples in different roasting-separation stages, where some peaks have been designated. The target elements  $\text{Fe}^+$ ,  $\text{Al}^+$ ,  $\text{Na}^+$ ,  $\text{Si}^+$ ,  $\text{Ti}^+$ ,  $\text{Ca}^+$ ,  $\text{K}^+$  and  $\text{Mg}^+$  all had positive ion fragment peaks. The peaks were extreme for the four elements  $\text{Na}^+$ ,  $\text{Al}^+$ ,  $\text{Fe}^+$  and  $\text{Ti}^+$ , indicating the abundance of these elements in the samples. A comparison of Figure 9a,b confirms that the peaks of  $\text{Si}^+$ ,  $\text{Al}^+$ ,  $\text{K}^+$ ,  $\text{Ca}^+$ ,  $\text{Ti}^+$  and other elements in the samples were significantly enhanced after roasting, indicating that the roasting process contributed to the activation of the ions in the raw ore.

Combined with Figure 9b–d, the elemental enrichment and migration patterns before and after magnetic separation can be evaluated. The positive ion fragment peak of  $\text{Na}^+$  changed significantly in the magnetic concentrate and magnetic tailings, and the peak intensity of  $\text{Na}^+$  after magnetic separation decreased to half of that in the roasted product (the value of  $10^n$  on the ordinate axis is used in the figure). This can be explained by the fact that the water flow in the magnetic separation process takes more than 50% of the free sodium in the sample.

The peak intensity of  $\text{Fe}^+$  in the magnetic concentrate was enhanced compared with that in the magnetic tailings, and the opposite is true for  $\text{Al}^+$ . In this case, it implies that although magnetic separation made the iron and aluminum minerals achieve effective separation to a certain extent, it failed to achieve complete and thorough separation of the two as a whole.

In the negative ion ToF-SIMS spectrum analysis, the ion fragment peak intensities of  $\text{O}^-$  and  $\text{OH}^-$  were more prominent in the four samples, while the intensities of  $\text{S}^-$  and  $\text{P}^-$

were relatively weak. As a confirmation of this, the chemical composition analysis and XRD results indicate that the elements of the samples were primarily present as oxides and hydroxides.

On the positive ion depth profile (Figure 11), the intensity of the ion signals versus sputtering time reflects the variation in the in-depth concentration [36–38]. The ion intensity is reported on a logarithmic scale. The figure shows that with increasing sputtering time and ion sputtering depth, the ion signal intensity of each element shows a trend of enhancement followed by smoothness, indicating a uniform distribution of elements within the samples. Nevertheless, the characteristic signals of  $\text{Na}^+$  in Figure 11A,D were found to be enhanced and then weakened, indicating that part of the  $\text{Na}^+$  elements adhered to the surface of the sample as free sodium, while another part existed inside the samples in the form of compounds.

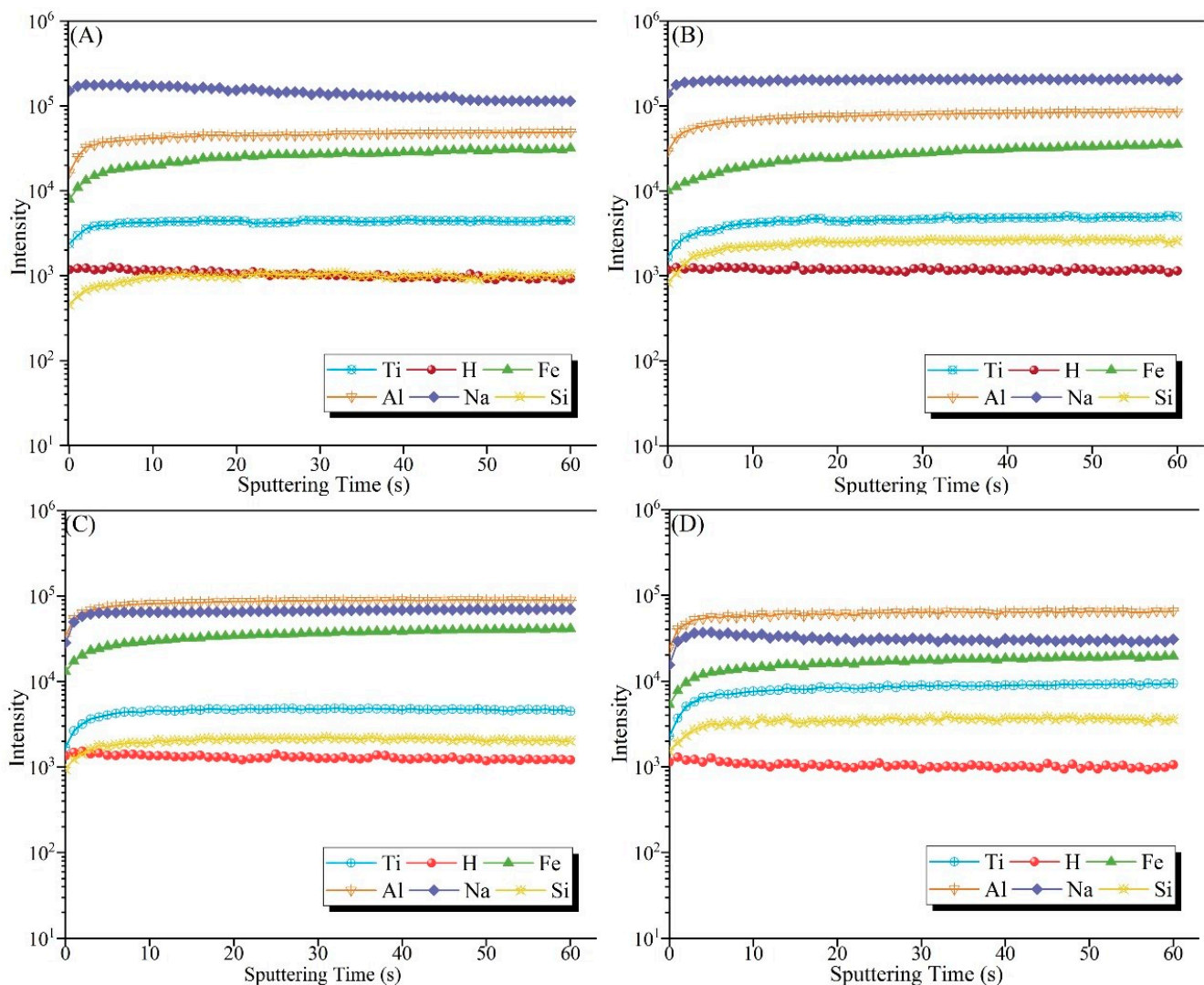
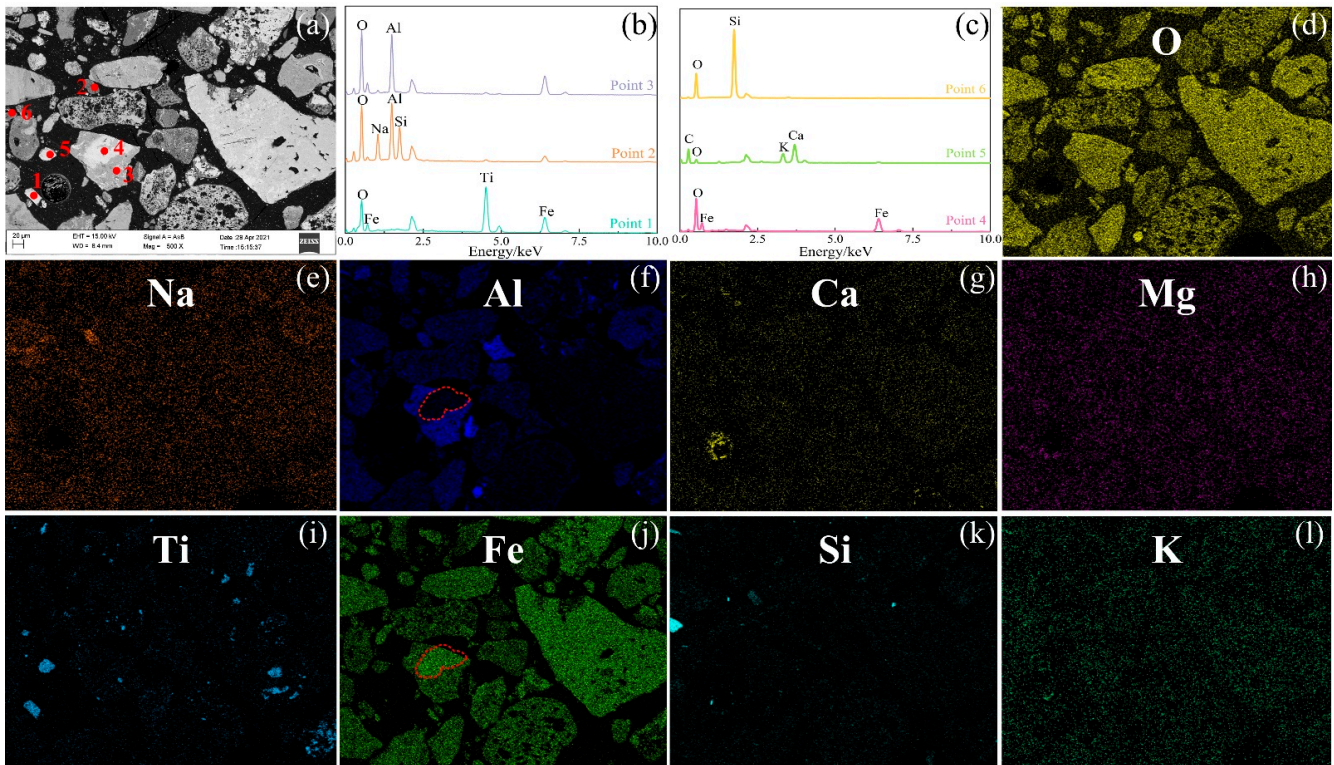


**Figure 11.** ToF-SIMS positive ion depth profiles for samples in different roasting-separation stages: (A) raw ore, (B) roasted product, (C) magnetic concentrate and (D) magnetic tailings.

The ion signal intensity of each metal element in the roasted product was also enhanced compared with those in the raw ore, which confirms that the roasting process has an activation effect on ions.

### 3.7. SEM-EDS Analysis

The microscopic morphology of the RM raw ore was illustrated by SEM-EDS analysis, as shown in Figure 12. With the combination of XRD, chemical composition and ToF-SIMS analysis, it could be determined that the raw ore primarily consisted of hematite and goethite in addition to small amounts of ilmenite, quartz, aluminosilicate mineral (High-Na), calcite, gibbsite and diaspore present.



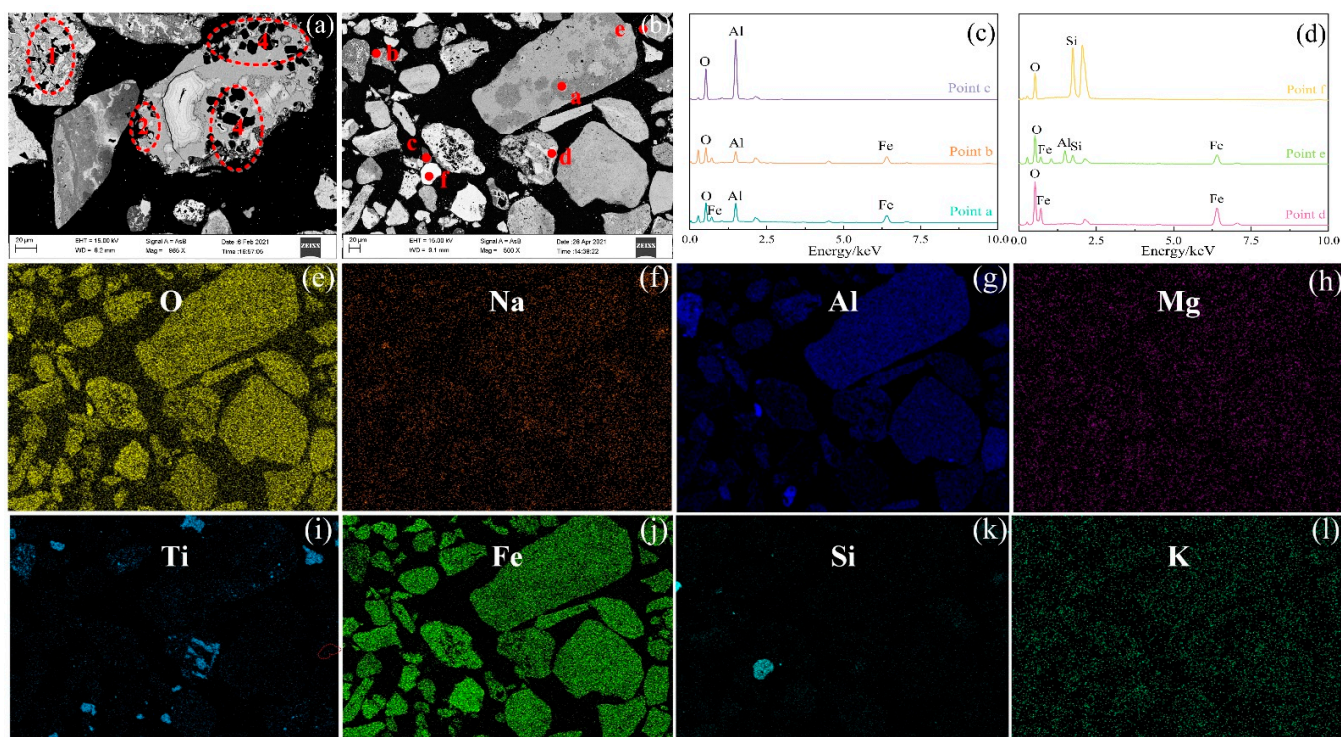
**Figure 12.** (a) SEM images; (b,c) EDS of points 1–6; (d–l) elemental mapping analysis of the raw ore.

Figure 12 shows an inlay of larger iron-mineral particles within the mineral grains of the gibbsite (points 3 and 4), together with several microscopic iron-mineral particles, which reveals the close relationship between iron and aluminum symbiosis. Ilmenite was essentially present as separate particles (points 1) and contained separately distributed quartz, calcite and sodium aluminosilicate (points 2, 5 and 6).

The roasted product's SEM images and EDS energy spectra are given in Figure 13. Figure 13a identifies the presence of more holes and cracks within the particles (areas 1, 2, 3 and 4), attributed to the removal of crystalline water from limonite to hematite, which was later reduced to magnetite by the reduction process.

It can be determined that the roasted product contained mainly magnetite (point d in Figure 13b) and Fe-Al spinel (points a and b) in addition to small amounts of ilmenite, quartz, corundum and other minerals. The gibbsite was dehydrated under the action of roasting to become  $\text{Al}_2\text{O}_3$  (point c in Figure 13b), and iron-aluminum oxides were distributed inside or on the surface of magnetite. It also contained separately distributed quartz and aluminosilicate mineral particles (points e and f).





**Figure 13.** (a,b) SEM images of the roasted product; (c,d) EDS of points a-f; (e–l) elemental mapping analysis of the roasted product.

#### 4. Conclusions

In this study, the feasibility of the mineral phase transformation-magnetic separation method for iron recovery from high-iron red mud was demonstrated. Under the roasting conditions of 560 °C roasting temperature, 20% CO concentration, 15 min roasting time and a total gas flow rate of 500 mL/min, a magnetic concentrate with an iron grade of 55.84% and recovery of 93.75% was obtained.

As indicated by the XRD, SEM-EDS and chemical composition analyses, iron minerals in the raw ore mainly existed in the form of hematite and goethite, which were transformed into magnetite through the roasting process and enriched in the magnetic concentrate by magnetic separation.

ToF-SIMS analysis revealed that the intensity of some elemental peaks in the roasted products was significantly enhanced with respect to the raw ore. The depth sputtering data demonstrate that the distribution of the elemental content within the particles was homogeneous, with only the Na signal weakening, indicating that some of the sodium was only attached to the surface of the mineral particles and existed in the form of free sodium.

**Author Contributions:** Conceptualization, S.Y.; writing—original draft, R.W.; resources, Y.L. and L.L.; data curation, H.Z.; writing—review and editing, S.Y. and Y.F. All authors have read and agreed to the published version of the manuscript.

**Funding:** This research was funded by the National Natural Science Foundation of China, under grant number 51904058, and the National Key Research and Development Program of China, under grant number 2018YFC1901902.

**Institutional Review Board Statement:** Not applicable.

**Informed Consent Statement:** Not applicable.

**Data Availability Statement:** The data presented in this study are available on request from the corresponding author.

**Conflicts of Interest:** The authors declare no conflict of interest.

## References

1. Liu, X.; Han, Y.; He, F.; Gao, P.; Yuan, S. Characteristic, hazard and iron recovery technology of red mud—A critical review. *J. Hazard Mater.* **2021**, *420*, 126542. [[CrossRef](#)] [[PubMed](#)]
2. Luo, Z.; Hao, Y.; Mu, Y.; Tang, C.; Liu, X. Solidification/stabilization of red mud with natural radionuclides in granular blast furnace slag based geopolymers. *Constr. Build. Mater.* **2022**, *316*, 125916. [[CrossRef](#)]
3. Ebrahimejad, M.; Karimzadeh, R. Hydrocracking and hydrodesulfurization of diesel over zeolite beta-containing NiMo supported on activated red mud. *Adv. Powder Technol.* **2019**, *30*, 1450–1461. [[CrossRef](#)]
4. Cheng, Y.; Xu, L.; Liu, C. NaP1 zeolite synthesized via effective extraction of Si and Al from red mud for methylene blue adsorption. *Adv. Powder Technol.* **2021**, *32*, 3904–3914. [[CrossRef](#)]
5. Liu, X.; Gao, P.; Yuan, S.; Lv, Y.; Han, Y. Clean utilization of high-iron red mud by suspension magnetization roasting. *Miner. Eng.* **2020**, *157*, 106553. [[CrossRef](#)]
6. Huang, Y.; Yang, H.; Li, K.; Meng, Q.; Wang, S.; Wang, Y.; Zhu, P.; Niu, Q.; Yan, H.; Li, X.; et al. Red mud conserved compost nitrogen by enhancing nitrogen fixation and inhibiting denitrification revealed via metagenomic analysis. *Bioresour. Technol.* **2022**, *346*, 126654. [[CrossRef](#)]
7. Arroyo, F.; Luna-Galiano, Y.; Leiva, C.; Vilches, L.F.; Fernández-Pereira, C. Environmental risks and mechanical evaluation of recycling red mud in bricks. *Environ. Res.* **2020**, *186*, 109537. [[CrossRef](#)]
8. Liu, W.; Chen, X.; Li, W.; Yu, Y.; Yan, K. Environmental assessment, management and utilization of red mud in China. *J. Clean Prod.* **2014**, *84*, 606–610. [[CrossRef](#)]
9. Luo, Z.; Zhi, T.; Liu, L.; Mi, J.; Zhang, M.; Tian, C.; Si, Z.; Liu, X.; Mu, Y. Solidification/stabilization of chromium slag in red mud-based geopolymer. *Constr. Build. Mater.* **2022**, *316*, 125813. [[CrossRef](#)]
10. Dong, M.; Ruan, S.; Zhan, S.; Shen, S.; Sun, G.; Qian, X.; Zhou, X. Utilization of red mud with high radiation for preparation of autoclaved aerated concrete (AAC): Performances and microstructural analysis. *J. Clean Prod.* **2022**, *347*, 131293. [[CrossRef](#)]
11. Milačič, R.; Zuliani, T.; Ščančar, J. Environmental impact of toxic elements in red mud studied by fractionation and speciation procedures. *Sci. Total Environ.* **2012**, *426*, 359–365. [[CrossRef](#)] [[PubMed](#)]
12. Khairul, M.A.; Zanganeh, J.; Moghtaderi, B. The composition, recycling and utilisation of Bayer red mud. *Resour. Conserv. Recycl.* **2019**, *141*, 483–498. [[CrossRef](#)]
13. Wang, S.; Jin, H.; Deng, Y.; Xiao, Y. Comprehensive utilization status of red mud in China: A critical review. *J. Clean Prod.* **2021**, *289*, 125136. [[CrossRef](#)]
14. Shao, S.; Zhang, P.; Xiang, X.; Li, X.; Zhang, H. Promoted ketonization of bagasse pyrolysis gas over red mud-based oxides. *Renew. Energy* **2022**, *190*, 11–18. [[CrossRef](#)]
15. Sahoo, P.; Sahoo, A. Hydrodynamic studies on fluidization of Red mud: CFD simulation. *Adv. Powder Technol.* **2014**, *25*, 1699–1708. [[CrossRef](#)]
16. Krivenko, P.; Kovalchuk, O.; Pasko, A.; Croymans, T.; Hult, M.; Lutter, G.; Vandevenne, N.; Schreurs, S.; Schroyers, W. Development of alkali activated cements and concrete mixture design with high volumes of red mud. *Constr. Build Mater.* **2017**, *151*, 819–826. [[CrossRef](#)]
17. Wang, L.; Yu, I.K.M.; Tsang, D.C.W.; Li, S.; Li, J.-s.; Poon, C.S.; Wang, Y.-S.; Dai, J.-G. Transforming wood waste into water-resistant magnesia-phosphate cement particleboard modified by alumina and red mud. *J. Clean Prod.* **2017**, *168*, 452–462. [[CrossRef](#)]
18. Liu, Y.; Naidu, R. Hidden values in bauxite residue (red mud): Recovery of metals. *Waste Manag.* **2014**, *34*, 2662–2673. [[CrossRef](#)]
19. Binnemans, K.; Jones, P.T.; Blanpain, B.; Van Gerven, T.; Pontikes, Y. Towards zero-waste valorisation of rare-earth-containing industrial process residues: A critical review. *J. Clean Prod.* **2015**, *99*, 17–38. [[CrossRef](#)]
20. Rao, D.S.; Rath, S.S.; Dash, N.; Mohanty, S.; Biswal, S.K. Mineralogy, liberation and leaching characteristics of iron oxide phases in an Indian diaspora sample. *T. Nonferr. Metal Soc.* **2018**, *28*, 1640–1651. [[CrossRef](#)]
21. Li, Y.; Wang, J.; Wang, X.; Wang, B.; Luan, Z. Feasibility study of iron mineral separation from red mud by high gradient superconducting magnetic separation. *Phys. C Supercond.* **2011**, *471*, 91–96. [[CrossRef](#)]
22. Jamieson, E.; Jones, A.; Cooling, D.; Stockton, N. Magnetic separation of Red Sand to produce value. *Miner. Eng.* **2006**, *19*, 1603–1605. [[CrossRef](#)]
23. Zhang, R.; Zheng, S.; Ma, S.; Zhang, Y. Recovery of alumina and alkali in Bayer red mud by the formation of andradite-grossular hydrogarnet in hydrothermal process. *J. Hazard Mater.* **2011**, *189*, 827–835. [[CrossRef](#)] [[PubMed](#)]
24. Yang, Y.; Wang, X.; Wang, M.; Wang, H.; Xian, P. Recovery of iron from red mud by selective leach with oxalic acid. *Hydrometallurgy* **2015**, *157*, 239–245. [[CrossRef](#)]
25. Li, W.; Yan, X.; Niu, Z.; Zhu, X. Selective recovery of vanadium from red mud by leaching with using oxalic acid and sodium sulfite. *J. Environ. Chem. Eng.* **2021**, *9*, 105669. [[CrossRef](#)]
26. Agrawal, S.; Rayapudi, V.; Dhawan, N. Extraction of Iron values from Red mud. *Mater. Today Proceed.* **2018**, *5*, 17064–17072. [[CrossRef](#)]
27. Liu, W.; Yang, J.; Xiao, B. Application of Bayer red mud for iron recovery and building material production from aluminosilicate residues. *J. Hazard Mater.* **2009**, *161*, 474–478. [[CrossRef](#)]
28. Zhang, Q.; Sun, Y.; Han, Y.; Li, Y.; Gao, P. Producing magnetite concentrate via self-magnetization roasting in N<sub>2</sub> atmosphere: Phase and structure transformation, and extraction kinetics. *J. Ind. Eng. Chem.* **2021**, *104*, 571–581. [[CrossRef](#)]



29. Tang, Z.; Zhang, Q.; Sun, Y.; Gao, P.; Han, Y. Pilot-scale extraction of iron from flotation tailings via suspension magnetization roasting in a mixture of CO and H<sub>2</sub> followed by magnetic separation. *Resour. Conserv. Recycl.* **2021**, *172*, 105680. [[CrossRef](#)]
30. Iatsunskiy, I.; Gottardi, G.; Micheli, V.; Canteri, R.; Coy, E.; Bechelany, M. Atomic layer deposition of palladium coated TiO<sub>2</sub>/Si nanopillars: ToF-SIMS, AES and XPS characterization study. *Appl. Surface Sci.* **2021**, *542*, 148603. [[CrossRef](#)]
31. Lai, H.; Deng, J.; Liu, Q.; Wen, S.; Song, Q. Surface chemistry investigation of froth flotation products of lead-zinc sulfide ore using ToF-SIMS and multivariate analysis. *Sep. Purif. Technol.* **2021**, *254*, 117655. [[CrossRef](#)]
32. Wang, L.; Voyshnis, S.; Seyeux, A.; Marcus, P. Ion transport mechanisms in the passive film formed on 304L stainless steel studied by ToF-SIMS with 18O isotopic tracer. *Corros. Sci.* **2020**, *173*, 108779. [[CrossRef](#)]
33. Ye, S.; Lin, J.-C.; Kang, L.-L.; Li, C.-L.; Hou, S.-S.; Lee, T.-L.; Chuang, S.-F. Investigations of silane-MDP interaction in universal adhesives: A ToF-SIMS analysis. *Dental Mater.* **2021**, *38*, 183–193. [[CrossRef](#)] [[PubMed](#)]
34. Cornette, P.; Zanna, S.; Seyeux, A.; Costa, D.; Marcus, P. The native oxide film on a model aluminium-copper alloy studied by XPS and ToF-SIMS. *Corros. Sci.* **2020**, *174*, 108837. [[CrossRef](#)]
35. Kia, A.M.; Speulmanns, J.; Bönhardt, S.; Emara, J.; Kühnel, K.; Haufe, N.; Weinreich, W. Spectroscopic analysis of ultra-thin TiN as a diffusion barrier for lithium-ion batteries by ToF-SIMS, XPS, and EELS. *Appl. Surface Sci.* **2021**, *564*, 150457. [[CrossRef](#)]
36. Gulin, A.; Shakhov, A.; Vasin, A.; Astafiev, A.; Antonova, O.; Kochev, S.; Kabachii, Y.; Golub, A.; Nadochenko, V. ToF-SIMS depth profiling of nanoparticles: Chemical structure of core-shell quantum dots. *Appl. Surface Sci.* **2019**, *481*, 144–150. [[CrossRef](#)]
37. Lai, H.; Liu, Q.; Deng, J.; Wen, S. Using ToF-SIMS to study metal ions transfer between chalcopyrite and galena during grinding. *Adv. Powder Technol.* **2020**, *31*, 2650–2657. [[CrossRef](#)]
38. Awasthi, S.; Gong, B.; Fuerbach, A.; Marjo, C.; Kane, D.M. ToF-SIMS of femtosecond laser irradiated muscovite with topography: Evidence of Na and K enrichment near the surface. *Appl. Surface Sci.* **2021**, *581*, 151746. [[CrossRef](#)]